The Astrophysical Journal Letters, 819:L7 (7pp), 2016 March 1 doi:10.3847/2041-8205/819/1/L7

ALMA OBSERVATIONS OF A GAP AND A RING IN THE PROTOPLANETARY DISK AROUND TW HYA

Hideko Nomura[1,13], Takashi Tsukagoshi[2,14], Ryohei Kawabe[3,4,5], Daiki Ishimoto[1,6], Satoshi Okuzumi[1], Takayuki Muto[7], Kazuhiro D. Kanagawa[8,9], Shigeru Ida[10], Catherine Walsh[11], T. J. Millar[12], and Xue-Ning Bai[13]

[1] Department of Earth and Planetary Sciences, Tokyo Institute of Technology, 2-12-1 Ookayama, Meguro, Tokyo, 152-8551, Japan; nomura@geo.titech.ac.jp
[2] College of Science, Ibaraki University, Mito, Ibaraki 310-8512, Japan
[3] National Astronomical Observatory of Japan, 2-21-1 Osawa, Mitaka, Tokyo 181-8588, Japan
[4] SOKENDAI (The Graduate University for Advanced Studies), 2-21-1 Osawa, Mitaka, Tokyo 181-8588, Japan
[5] Department of Astronomy, School of Science, University of Tokyo, Bunkyo, Tokyo 113-0033, Japan
[6] Department of Astronomy, Graduate School of Science, Kyoto University, Kitashirakawa-Oiwake-cho, Sakyo-ku, Kyoto 606-8502, Japan
[7] Division of Liberal Arts, Kogakuin University, 1-24-2 Nishi-Shinjuku, Shinjuku-ku, Tokyo, 163-8677, Japan
[8] Institute of Low Temperature Science, Hokkaido University, Sapporo 060-0819, Japan
[9] Institute of Physics and CASA*, Faculty of Mathematics and Physics, University of Szczecin, Wielkopolska 15, 70-451 Szczecin, Poland
[10] Earth-Life Science Institute, Tokyo Institute of Technology, 2-12-1 Ookayama, Meguro, Tokyo 152-8550, Japan
[11] Leiden Observatory, Leiden University, P.O. Box 9513, 2300 RA Leiden, The Netherlands
[12] Astrophysics Research Centre, School of Mathematics and Physics, Queen's University Belfast, University Road, Belfast BT7 1NN, UK
[13] Institute for Theory and Computation, Harvard-Smithsonian Center for Astrophysics, 60 Garden Street, MS-51, Cambridge, MA 02138, USA
Received 2015 December 16; accepted 2016 February 5; published 2016 February 24

ABSTRACT

We report the first detection of a gap and a ring in 336 GHz dust continuum emission from the protoplanetary disk around TW Hya, using the Atacama Large Millimeter/Submillimeter Array (ALMA). The gap and ring are located at around 25 and 41 au from the central star, respectively, and are associated with the CO snow line at ~30 au. The gap has a radial width of less than 15 au and a mass deficit of more than 23%, taking into account that the observations are limited to an angular resolution of ~15 au. In addition, the ^{13}CO and C^{18}O $J = 3 - 2$ lines show a decrement in CO line emission throughout the disk, down to ~10 au, indicating a freeze-out of gas-phase CO onto grain surfaces and possible subsequent surface reactions to form larger molecules. The observed gap could be caused by gravitational interaction between the disk gas and a planet with a mass less than super-Neptune ($2M_{\rm Neptune}$), or could be the result of the destruction of large dust aggregates due to the sintering of CO ice.

Key words: molecular processes – planet–disk interactions – protoplanetary disks – stars: individual (TW Hya) – submillimeter: planetary systems

1. INTRODUCTION

The physical structures and chemical compositions of gas, dust, and ice in protoplanetary disks control the formation processes of planets and the compositions of their cores and atmospheres. The Atacama Large Millimeter/Submillimeter Array (ALMA) long baseline campaign has detected gaps and rings in dust continuum emission from the circumstellar disk around a very young star (~0.1–1 Myr), HL Tau (ALMA Partnership et al. 2015). The origin of this complex disk structure in such a young object remains under debate.

In this Letter, we present ALMA observations of the relatively old (~3–10 Myr) gas-rich disk around the young Sun-like star, TW Hya (~$0.8M_\odot$), which show the presence of a gap and a ring associated with the CO snow line. TW Hya's proximity (54 ± 6 pc) makes it an ideal source for studying the formation environment of a planetary system (e.g., Andrews et al. 2012). The disk is old compared with other gas-rich protoplanetary disks, whose lifetimes are typically ~3 Myr (e.g., Hernández et al. 2007). Nevertheless, the disk gas mass is $>0.05M_\odot$, inferred through HD line observations with *Herschel* (Bergin et al. 2013). In exoplanetary systems giant planets have been discovered at/beyond Neptune orbits around Sun-like stars by direct imaging observations using Subaru/HiCIAO (Thalmann et al. 2009; Kuzuhara et al. 2013). Thus, planets are able to form even at large distances within disk lifetimes by, for example, scattering of planetary cores (Kikuchi et al. 2014). Given that planet–disk interaction is key for planet orbital evolution and planet population synthesis (e.g., Kley & Nelson 2012; Ida et al. 2013), understanding gap formation in protoplanetary disks helps us to gain insight into the early evolution of our own solar system, as well as the observed diversity of exoplanetary systems.

2. OBSERVATIONS AND DATA REDUCTION

TW Hya was observed with ALMA in Band 7 on 2015 May 20–21 with 40 antennas in Cycle 2 with a *uv*-coverage of 22–580 kλ (PI: D. Ishimoto). The spectral windows were centered at 329.295 GHz (SPW1), 330.552 GHz (SPW0), 340.211 GHz (SPW2), and 342.846 GHz (SPW3), covering C^{18}O $J = 3 - 2$, ^{13}CO $J = 3 - 2$, CN $N = 3 - 2$, and CS $J = 7 - 6$. The channel spacing was $\delta\nu = 30.52$ kHz and the bandwidth was 117.188 MHz, except for SPW2, in which a channel spacing of $\delta\nu = 15.26$ kHz and a bandwidth of 58.594 MHz were used. The quasar J1058+0133 was observed as a bandpass calibrator, while the nearby quasar J1037-2934 was used for phase and gain calibration. The mean flux density of J1037-2934 was 0.58 Jy during the observation period.

The visibility data were reduced and calibrated using CASA, versions 4.3.1 and 4.4.0. The visibility data were separately reduced for each SPW, and the continuum visibilities were extracted by averaging the line-free channels in all SPWs. The corrected visibilities were imaged using the CLEAN algorithm with Briggs weighting with a robust parameter of 0 after calibration of the bandpass, gain in amplitude and phase, and absolute flux scaling, and then flagging for aberrant data. In addition to the usual CLEAN imaging, we performed self-

[14] These authors contributed equally to this work.

calibration of the continuum emission to improve the sensitivity and image quality. The obtained solution table of the self-calibration for the continuum emission was applied to the visibilities of the lines. The self-calibration significantly improved the sensitivity of the continuum image by one order of magnitude from 2.6 to 0.23 mJy. In addition, the continuum visibility data with deprojected baselines longer than 200 kλ were extracted in order to enhance small-scale structure around the gap. The high spatial resolution data were analyzed in a similar way, but were imaged using the CLEAN algorithm with uniform weighting. Also, the ALMA archived data of the N_2H^+ $J = 4 - 3$ line at 372.672 GHz were reanalyzed in a similar way to compare with the data obtained by our observations. The reanalyzed data is consistent with that in Qi et al. (2013). For the N_2H^+ line data, the synthesized beam and the 1σ rms noise level in 0.1 km s^{-1} were $0\farcs44 \times 0\farcs41$ (P.A. = $12\fdg4$) and 31.2 mJy beam^{-1}.

3. RESULTS

3.1. Dust Continuum Emission

The observed dust continuum emission maps at 336 GHz are plotted for both the full data (Figure 1(a)) and high spatial frequencies only (>200 kλ, Figure 1(b)). The synthesized beam and rms noise were $0\farcs37 \times 0\farcs31$ (~20 au, P.A. = $55\fdg7$) and 0.23 mJy beam^{-1}. The total and peak flux density were 1.41 Jy and 0.15 Jy beam^{-1}, with signal-to-noise ratios (S/N) of 705 and 652, respectively. The results agree well with the previous SMA observations (Andrews et al. 2012) and ALMA observations (Hogerheijde et al. 2016) with lower spatial resolution and sensitivity. The synthesized beam and rms for the data at high spatial resolution data only were $0\farcs32 \times 0\farcs26$ (~15 au, P.A. = $54\fdg5$) and 0.49 mJy beam^{-1}.

As shown by the black line in Figure 2(a), the dust continuum emission of the full data has a shallow dip in the radial profile of the surface brightness obtained by deprojecting the observed image data assuming an inclination angle of 7° and a position angle of −30° (Qi et al. 2008). By imaging the data at high spatial frequencies only (>200 kλ), we identify a gap and a ring at around 25 and 41 au, respectively (Figure 1(b) and gray line in Figure 2(a)). The *uv*-coverage of the full data set (from 22 to 580 kλ) is sufficiently high and indeed vital for this analysis. The continuum visibility profile as a function of the deprojected baseline length is plotted in Figure 3. Our result is consistent with the recent ALMA observations with higher spatial resolution and sensitivity (Zhang et al. 2016). Since the high spatial frequency data miss the flux of spatially extended structure, the total flux is lower than that of the full data by an order of magnitude. Artificial structure appears at $R > 70$ au in the high spatial frequency data, probably due to a failure to subtract the side lobe pattern of the synthesized beam. Its intensity is less than the 2σ noise level and the structure is masked in Figure 2(a). The location of the gap is similar to that of the axisymmetric depression in polarized intensity of near-infrared scattered light imaging of dust grains recently found by Subaru/HiCIAO and *Gemini*/GPI (Akiyama et al. 2015; Rapson et al. 2015).

3.2. Dust Surface Density and Gap Parameters

We extract the radial dust surface density distribution (Figure 2(b)), using the deprojected data of the dust continuum emission and the equation,

$$I_{d,\nu} = B_\nu(T_d)[1 - \exp(-\tau_{d,\nu})], \tag{1}$$

where $I_{d,\nu}$ is the observed intensity of the dust continuum emission at the frequency ν, and $B_\nu(T_d)$ is the Planck function at the dust temperature, T_d. The optical depth, $\tau_{d,\nu}$, is defined as $\tau_{d,\nu} = \kappa_\nu \Sigma_{\rm dust}$, where $\Sigma_{\rm dust}$ is the dust surface density and the dust opacity, κ_ν, is set as $\kappa_\nu = 3.4\ {\rm cm^2\ g^{-1}}$. We adopt $T_d = 22\ {\rm K}(R/10\ {\rm au})^{-0.3}$, where R is the disk radius, by fitting the model result in Andrews et al. (2012) and assume a uniform temperature distribution in the vertical direction. The derived dust optical depth is shown in Figure 2(c). We note that the derived dust surface density distribution is consistent with that derived from SMA observations of dust continuum emission and model calculations (Andrews et al. 2012). Also, the assumed dust temperature is consistent with the color temperature obtained from the spectral index of continuum emission across the observed four basebands between 329 and 343 GHz (Figure 2(d)) in the optically thick regions (⩽30 au, Figure 2(c)).

To estimate the gap width, $\Delta_{\rm gap}$, and depth, $(\Sigma_0 - \Sigma)/\Sigma_0$, where Σ_0 and Σ are the basic surface density and the surface density with the gap at the gap center, the intensity at the gap, $I_{\rm gap}$ (red crosses in Figure 2(a)), is derived by completing the missing flux of the high spatial frequency data, $I_{\rm gap}^{\rm high}$ (gray line in Figure 2(a)), with the full spatial frequency data, $I^{\rm full}$ (black line in Figure 2(a)). The intensity profile across the gap was obtained as follows: (i) fit the high-frequency data without the gap using a power-law profile of $I_0^{\rm high} = 1.1 \times 10^3 R_{\rm au}^{-1.5}$ mJy beam^{-1}, (ii) fit the gap region in the high-frequency data using a single Gaussian profile of $\Delta I_{\rm gap} = I_0^{\rm high} - I_{\rm gap}^{\rm high} = 7.7 \exp(-(R_{\rm au} - 24.7\ {\rm au})^2/\{2(5.9\ {\rm au})^2\})$ mJy beam^{-1} (whose FWHM is 13.9 ± 1.0 au and depth is 7.7 ± 0.5 mJy) (green line in Figure 2(a)), and (iii) obtain the intensity at the gap as $I_{\rm gap} = I^{\rm full} - \Delta I_{\rm gap}$, where $I^{\rm full}$ is the intensity of the full data. In this fitting, we adopted the edges of the gap at R = 9–13 au (inner edge) and 39–43 au (outer edge) so that $\Delta I_{\rm gap}$ is overlaid to $I^{\rm full}$ smoothly. The optical depth at the gap is derived using $I_{\rm gap}$ and Equation (1), and then the dust surface density at the gap is derived using the same method mentioned above (red crosses in Figure 2(b)). The resulting gap width is $\Delta_{\rm gap} \sim 15$ au and the depth is $(\Sigma_0 - \Sigma)/\Sigma_0 \sim 0.23$. We note that our estimate of the gap width is limited by the angular resolution of the high spatial frequency data. The pattern of the gap and ring is also affected by residual artifacts due to the cutoff at 200 kλ, which introduces uncertainties in the location of the gap center, and the width and depth of the gap.

3.3. CO Isotopologue Line Emission

The observed ^{13}CO and C^{18}O $J = 3 - 2$ rotational line emission maps are plotted in Figures 1(c) and (d). The resulting synthesized beam and the 1σ rms noise level in the 0.03 km s^{-1} width-channels were $0\farcs41 \times 0\farcs33$ (P.A. = $53\fdg4$), 12.0 mJy beam^{-1} (^{13}CO), and $0\farcs41 \times 0\farcs33$ (P.A. = $53\fdg8$), 13.4 mJy beam^{-1} (C^{18}O). The integrated intensity maps were created by integrating from 1.18 to 4.30 km s^{-1} (^{13}CO) and from 1.48 to 4.15 km s^{-1} (C^{18}O). The resulting noise levels of the map were 8.4 mJy beam^{-1} km s^{-1} (^{13}CO) and 6.5 mJy beam^{-1} km s^{-1} (C^{18}O). The deprojected radial profiles

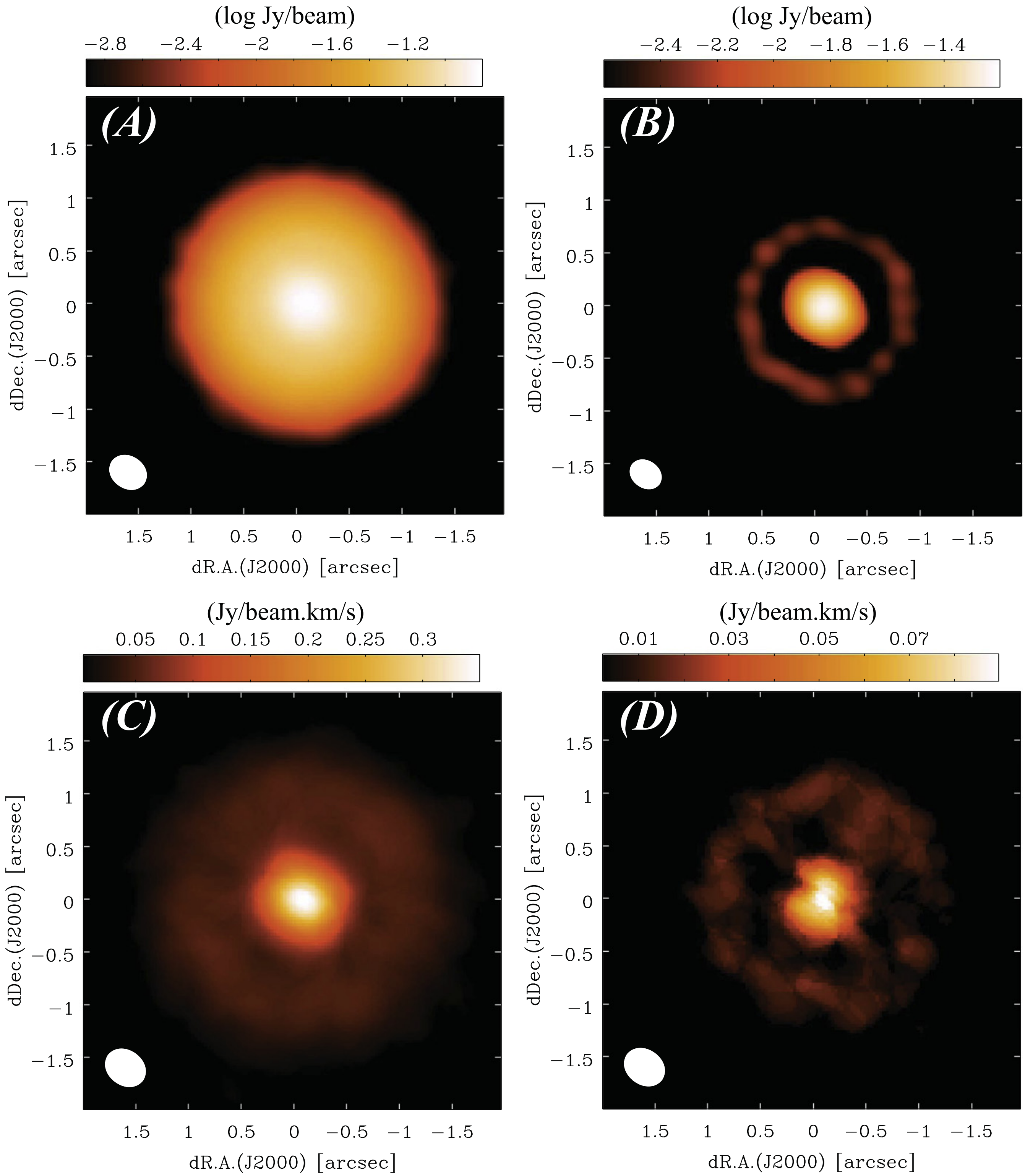

Figure 1. 336 GHz dust continuum map imaged using (A) all spatial frequency data, (B) only high spatial frequency (>200 kλ) data, and (C) ^{13}CO $J = 3 - 2$ and (D) C^{18}O $J = 3 - 2$ integrated line emission maps. Emission that was less than the 5σ noise level were masked. The synthesized beam sizes are shown in the bottom left corner of each panel.

of the integrated line emission of the ^{13}CO and C^{18}O following the subtraction of the dust continuum emission are plotted in Figure 4(a). The S/N is not sufficiently high enough to analyze the high spatial resolution data.

3.4. CO Column Density

We obtain the CO radial column density distribution, using the deprojected data of the ^{13}CO and C^{18}O line observations (Figure 4(d)). The CO column density, $N_{\rm CO}$, is derived from the

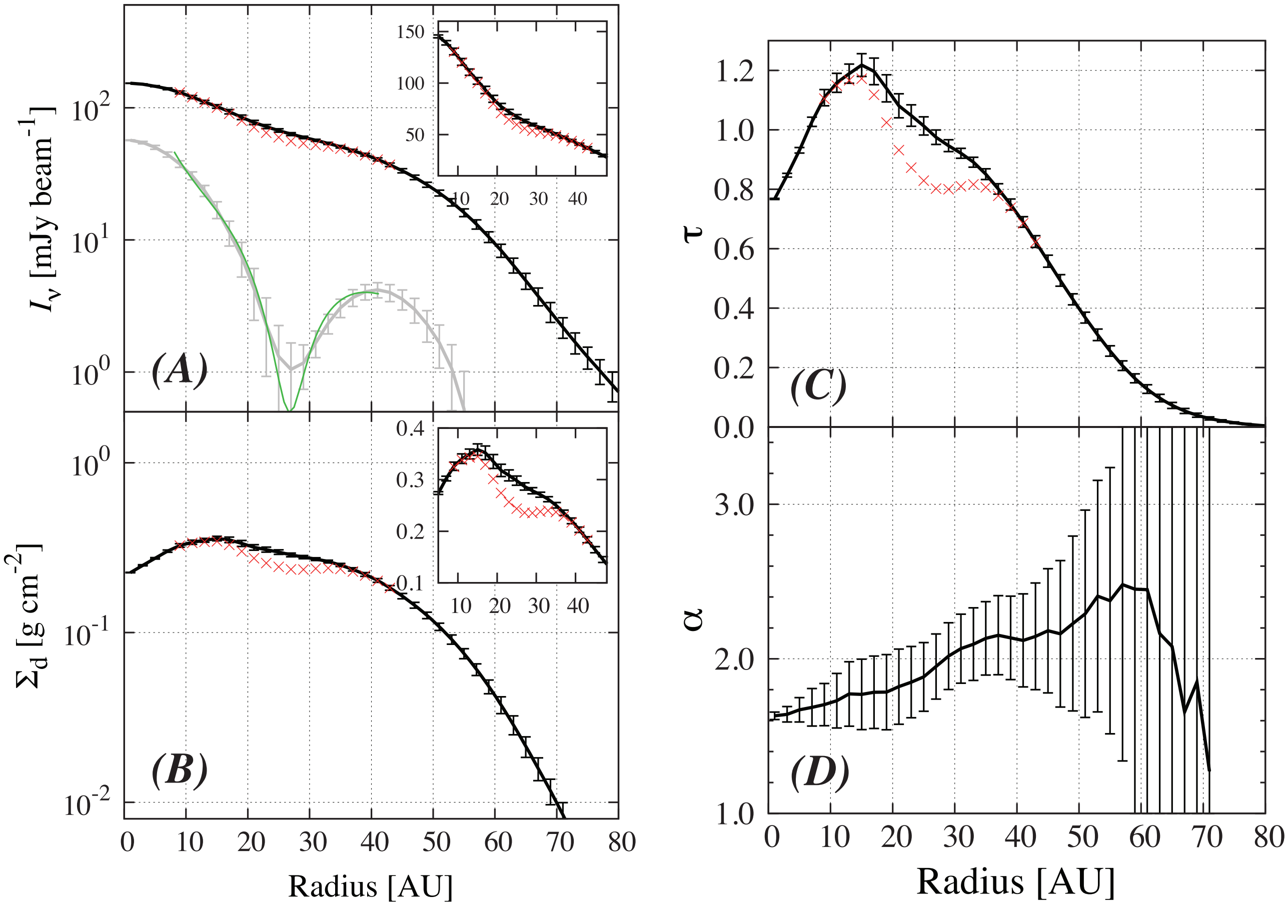

Figure 2. Radial distributions of (A) intensity of 336 GHz dust continuum emission, (B) dust surface density, (C) optical depth, and (D) spectral index between 329 and 343 GHz. The gray line in Figure (A) shows the data of only high spatial frequency with its Gaussian fit (green line). Red crosses in (A)–(C) are derived from high spatial frequency data recovered by the full spatial frequency data at the gap. The inserts show a close-up of the region around the gap.

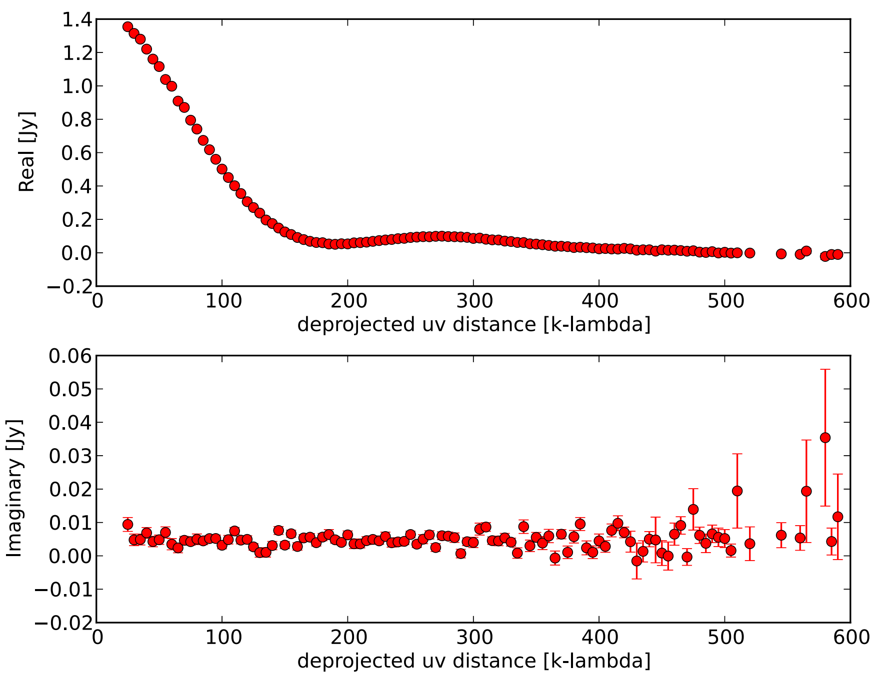

Figure 3. Real (top) and imaginary (bottom) parts of the azimuthally averaged continuum visibility profile as a function of the deprojected baseline length.

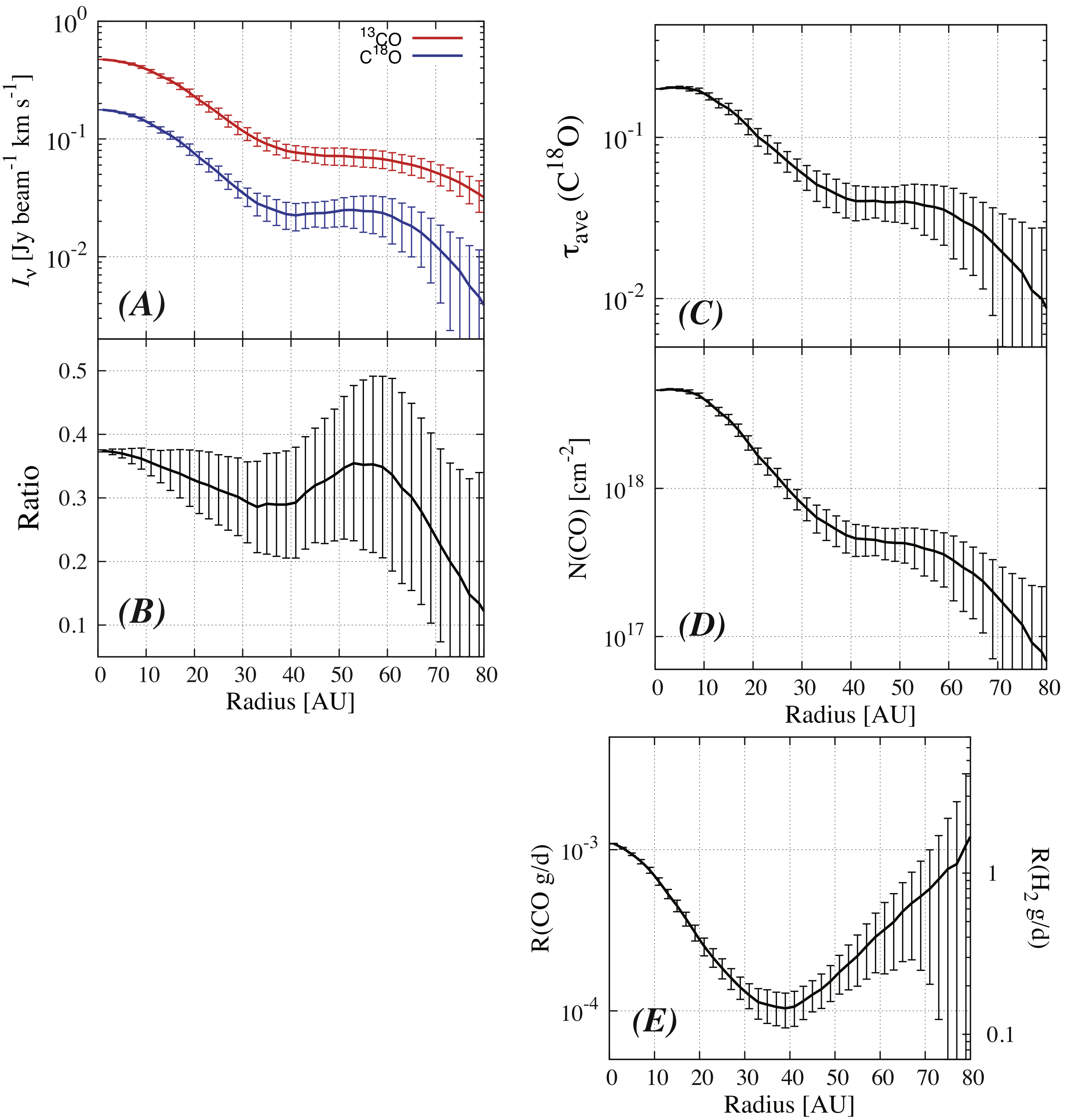

Figure 4. Radial distributions of (A) the integrated line emission of ^{13}CO (red line) and C^{18}O (blue line) $J = 3 - 2$, (B) the line ratio of C^{18}O to ^{13}CO, (C) the averaged optical depth of the C^{18}O line, (D) the CO column density, and (E) the CO gas-to-dust surface density ratio. The H_2 gas-to-dust ratio is also marked as a reference by simply assuming the abundance ratio of CO to H_2 to be 6×10^{-5}. All data are smoothed to a beam size of $0\farcs45 \times 0\farcs45$.

integrated line emission of C^{18}O $J = 3 - 2$ (Rybicki & Lightman 1979; Turner 1991), assuming abundance ratios of CO:^{13}CO = 67:1 and ^{13}CO:C^{18}O = 7:1 (Qi et al. 2011). The optical depth of the C^{18}O line emission, $\tau_{\rm C^{18}O,\nu}$ (Figure 4(c)), is obtained from the observed line intensity as follows. We assume that the CO line-emitting region is mainly in the surface layer, while the dust continuum-emitting region is near the midplane. Thus, the deprojected intensity of the CO line emission plus dust continuum emission can be approximately derived from the following equation by simply assuming three zones in the vertical direction of the disk,

$$\begin{aligned} I_{\rm C^{18}O+cont,\nu} = & B_\nu(T_g)(1 - e^{-\tau_{\rm C^{18}O,\nu}/2}) \\ & + B_\nu(T_d)(1 - e^{-\tau_{d,\nu}})e^{-\tau_{\rm C^{18}O,\nu}/2} \\ & + B_\nu(T_g)(1 - e^{-\tau_{\rm C^{18}O,\nu}/2})e^{-\tau_{d,\nu}-\tau_{\rm C^{18}O,\nu}/2}, \end{aligned} \quad (2)$$

where T_g is the gas temperature of the CO line-emitting region and T_d is the dust temperature near the midplane. The continuum-subtracted data, $I_{\rm C^{18}O+cont,\nu} - I_{d,\nu}$, together with Equation (1) are used for the analysis. Since the observed line

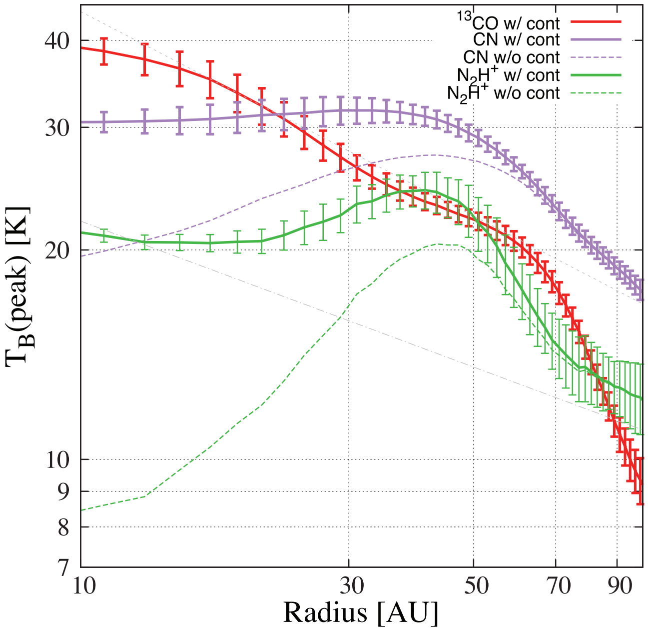

Figure 5. Radial distributions of the observed brightness temperature at the peak of ^{13}CO $J = 3 - 2$ (red) and $N_2H^+ J = 4 - 3$ (green) lines. The dust temperature at the midplane (dotted–dashed gray line) and the brightness temperature of the CN $N = 3 - 2$ (purple) line are also plotted for comparison. Dashed lines show the data subtracted by the dust continuum emission for N_2H^+ and CN. All data are smoothed to a beam size of $0\farcs45 \times 0\farcs45$.

ratio of $\int I_{C^{18}O,\nu} dv / \int I_{^{13}CO,\nu} dv$ is larger than 1/7 (Figure 4(b)), the ^{13}CO line is optically thick. Therefore, we adopt the brightness temperature at the peak of the ^{13}CO line (Figure 5) as the gas temperature, T_g. Also, we adopt a dust temperature of $T_d = 22\,\mathrm{K}(R/10\,\mathrm{au})^{-0.3}$ and the dust optical depth, $\tau_{d,\nu}$, is derived from the dust continuum observations (Figure 2(c)). We note that in the analysis we simply assume that the gas temperature is uniform in the vertical direction, and the gas temperature of the $C^{18}O$ line-emitting region is the same as that of the ^{13}CO line-emitting region, although it could be lower in reality. In addition, $C^{18}O$ could be depleted due to the effect of isotopologue-dependent photodissociation, and $N_{CO}/N_{C^{18}O}$ is possibly higher than 440 (Miotello et al. 2014). The CO column density will be underestimated due to these effects.

3.5. CO Gas-to-dust Surface Density Ratio

Using the obtained CO column density and dust surface density (Figures 4(d) and 2(b)), we derive the CO gas-to-dust surface density ratio (Figure 4(e)). If we convert it to the H_2 surface density, assuming an abundance ratio of CO to H_2 of 6×10^{-5} (Qi et al. 2011), the estimated H_2 gas mass is orders of magnitude lower than that predicted from the observations of the HD line emission by the *Herschel Space Observatory* (Bergin et al. 2013). The resulting H_2 gas-to-dust surface density ratio (∼0.1–1) is about two orders of magnitude lower than the typical interstellar value of ∼100, which suggests strong CO depletion throughout the disk down to ∼10 au.

The CO gas-to-dust surface density ratio increases beyond a radius of ∼40 au since the dust surface density drops dramatically in this region. It could be due to the drift of pebbles from the outer disk toward the central star (e.g., Takeuchi et al. 2005; Andrews et al. 2012; Walsh et al. 2014b).

4. DISCUSSIONS

4.1. Origin of the Gap and Ring in the Dust Continuum Emission

The gap and ring resemble those in the HL Tau system, recently found by the ALMA long baseline campaign (ALMA Partnership et al. 2015). Our result shows that gaps and rings in the (sub)millimeter dust continuum can exist, not only in relatively young disks (0.1–1 Myr) but also in relatively old disks (3–10 Myr). One possible mechanism for opening a gap is the gravitational interaction between a planet and the gas (e.g., Lin & Papaloizou 1979; Goldreich & Tremaine 1980; Fung et al. 2014). Such an interaction may also produce the spiral density waves recently found in optical and near-infrared scattered light imaging of dust grains in protoplanetary disks (e.g., Muto et al. 2012). According to recent theoretical analyses of gap structure around a planet (Kanagawa et al. 2015a, 2015b, 2016), the depth and width of the gap are controlled by the planetary mass, the turbulent viscosity, and the gas temperature. The shape of the gap is strongly influenced by angular momentum transfer via turbulent viscosity and/or instability caused by a steep pressure gradient at the edges of a gap. The observed gap has an apparent width and depth of $\Delta_{gap} \sim 15$ au and $(\Sigma_0 - \Sigma)/\Sigma_0 \sim 0.23$, respectively. This is too shallow and too wide compared with that predicted by theory. However, the observations are limited to an angular resolution of ∼15 au, and the depth and width could be deeper and narrower in reality. For instance, if we assume that the gap depth times the gap width retains the value derived from the observations, it is possible for the gap to have a width and depth of $\Delta_{gap} \sim 6$ au and $(\Sigma_0 - \Sigma)/\Sigma_0 \sim 0.58$, which is similar to the GPI result (Rapson et al. 2015). Such a gap could be opened by a super-Neptune-mass planet, depending on the parameters of the disk, such as the turbulent viscosity (Kanagawa et al. 2015a, 2015b, 2016). If the gap in the larger dust grains is deeper than that in the gas, the planet could be lighter than super-Neptune mass. We note that a planet of even a few Earth masses, although it cannot open a gap in the gas, can open a gap in the dust distribution if a certain amount of pebble-sized particles, whose motions are not perfectly coupled to that of gas, are scattered by the planet and/or the spiral density waves excited by the planet (Paardekooper & Mellema 2006; Muto & Inutsuka 2009).

Another possible mechanism to form a gap and an associated ring in dust continuum emission is the microscopic process of sintering CO ice on dust aggregates (Sirono 2011; Okuzumi et al. 2016). The gaps and rings observed in the younger and more luminous HL Tau system could be explained by the sintering of various molecular ices in the disk at their distinct snow line locations (Okuzumi et al. 2016). Although our observations indicate that the CO-depleted region is located down to ∼10 au in the TW Hya system, model calculations of the temperature in the disk suggest that the CO snow line is located at ∼30 au. Sintering is a process that renders an aggregate less sticky (Sirono 2011). Just outside the CO snow line where sintering occurs, large aggregates are easily destroyed, becoming small fragments through collisions, and their radial drift motion by the above-mentioned mechanism slows down. Thus, dust grains are stuck just outside the CO snow line, and a bright ring and a dark lane inside the ring is formed in the dust continuum emission. If another sintering region is formed inside the dark lane by, for example, CH_4 sintering, the region between the bright CO and CH_4 sintering regions would look like a gap. According to model calculations (Okuzumi et al. 2016), the CH_4 sintering region is located at ∼10 au in the TW Hya disk.

4.2. *CO Gas Depletion Inside the CO Snow Line*

From the CO line observations, we find a very low column density of CO compared with dust throughout the disk, down to a radius of about 10 au. This CO depletion could indicate a general absence of H_2 gas compared with dust. However, the *Herschel* HD observations (Bergin et al. 2013) indicates that it is more likely that it is due to CO freeze-out on grains with the possibility that subsequent grain-surface reactions form larger molecules even inside the CO snow line (Favre et al. 2013; Williams & Best 2014). The CO column density derived from our observations, $N_{\rm CO} \sim 10^{18}\,{\rm cm}^{-2}$, can be explained by detailed model calculations using a chemical network that includes freeze-out of molecules on grains and grain-surface reactions (Aikawa et al. 2015). The model calculations show that the CO depletion will proceed inside the CO snow line due to the sink effect: conversion of CO to less volatile species on grain surfaces. In the case of TW Hya, it could occur on a timescale shorter than the disk lifetime, depending on the amount of small grains. See Aikawa et al. (2015) for more detailed discussions, including the effect on other species. The CO depletion spread over the disk is inconsistent with the prediction by the previous ALMA N_2H^+ observations that depletion would be localized beyond the CO snow line (Qi et al. 2013). This could be because the N_2H^+ line emission traces the disk surface and not the CO-depleted region.

Figure 5 shows the brightness temperature at the peak of the ^{13}CO $J = 3 - 2$ line obtained by our observations and the N_2H^+ $J = 4 - 3$ line at 372.672 GHz obtained by the ALMA archived data (2011.0.00340.S). Since the ^{13}CO line is optically thick, the brightness temperature at the peak of the line emission represents the gas temperature of the line-emitting region. If LTE is applicable, the N_2H^+ brightness temperature is higher than the gas temperature of the ^{13}CO line-emitting region at the disk radius of ∼40 au, and higher than the dust temperature near the midplane down to ∼15 au (Figure 5). If the N_2H^+ line is optically thin, the gas temperature of the line-emitting region is higher than the brightness temperature. Therefore, the N_2H^+ line should come from the surface layer of the disk. Model calculations also predict that N_2H^+ exists in the disk surface for the model with (sub)micron-sized grains, similar to radical species abundant in the disk surface, such as CN and C_2H (e.g., Walsh et al. 2010; Aikawa et al. 2015). Our results (Figure 5) and the SMA observations of C_2H (Kastner et al. 2015) show that the radial intensity profiles of these species are similar. They have peaks around the disk radius of 40 au, beyond which the dust surface density drops. The result suggests that in order to trace the CO-depleted region, the $C^{18}O$ line may be more robust than the N_2H^+ line.

In the CO-depleted region, complex organic molecules would be produced via grain-surface reactions because hydrogen attachment to CO is thought to produce methanol and more complex species (e.g., Watanabe & Kouchi 2008; Walsh et al. 2014a). Methyl cyanide, which has recently been detected from a protoplanetary disk for the first time by ALMA (Öberg et al. 2015), could be formed through such grain-surface reactions.

We would like to thank the referee for comments that improved our paper. We are also grateful to Sean Andrews and Joel Kastner for their fruitful comments. This paper makes use of the following ALMA data: ADS/JAO.ALMA#2013.1.01397.S and ADS/JAO.ALMA#2011.0.00340.S. ALMA is a partnership of ESO (representing its member states), NSF (USA), and NINS (Japan), together with NRC (Canada), NSC, ASIAA (Taiwan), and KASI (Republic of Korea), in cooperation with the Republic of Chile. The Joint ALMA Observatory is operated by ESO, AUI/NRAO, and NAOJ. This work is partially supported by Grants-in-Aid for Scientific Research 23103005, 25108004, 25400229, and 15H03646. T.T. was supported by JSPS KAKENHI grant No. 23103004. C.W. is supported by the Netherlands Organisation for Scientific Research (program number 639.041.335). Astrophysics at QUB is supported by a grant from the STFC.

Facility: ALMA.

REFERENCES

Aikawa, Y., Furuya, K., Nomura, H., & Qi, C. 2015, ApJ, 807, 120
Akiyama, E., Muto, T., Kusakabe, N., et al. 2015, ApJL, 802, L17
ALMA Partnership, Brogan, C. L., Pérez, L. M., et al. 2015, ApJL, 808, L3
Andrews, S. M., Wilner, D. J., Hughes, A. M., et al. 2012, ApJ, 744, 162
Bergin, E. A., Cleeves, L. I., Gorti, U., et al. 2013, Natur, 493, 644
Favre, C., Cleeves, L. I., Bergin, E. A., Qi, C., & Blake, G. A. 2013, ApJL, 776, L38
Fung, J., Shi, J.-M., & Chiang, E. 2014, ApJ, 782, 88
Goldreich, P., & Tremaine, S. 1980, ApJ, 241, 425
Hernández, J., Hartmann, L., Megeath, T., et al. 2007, ApJ, 662, 1067
Hogerheijde, M. R., Bekkers, D., Pinilla, P., et al. 2016, A&A, 589, A99
Ida, S., Lin, D. N. C., & Nagasawa, M. 2013, ApJ, 775, 42
Kanagawa, K. D., Muto, T., Tanaka, H., et al. 2015a, ApJL, 806, L15
Kanagawa, K. D., Muto, T., Tanaka, H., et al. 2016, PASJ, submitted
Kanagawa, K. D., Tanaka, H., Muto, T., Tanigawa, T., & Takeuchi, T. 2015b, MNRAS, 448, 994
Kastner, J. H., Qi, C., Gorti, U., et al. 2015, ApJ, 806, 75
Kikuchi, A., Higuchi, A., & Ida, S. 2014, ApJ, 797, 1
Kley, W., & Nelson, R. P. 2012, ARA&A, 50, 211
Kuzuhara, M., Tamura, M., Kudo, T., et al. 2013, ApJ, 774, 11
Lin, D. N. C., & Papaloizou, J. 1979, MNRAS, 186, 799
Miotello, A., Bruderer, S., & van Dishoeck, E. F. 2014, A&A, 572, A96
Muto, T., & Inutsuka, S.-i. 2009, ApJ, 695, 1132
Muto, T., Grady, C. A., Hashimoto, J., et al. 2012, ApJL, 748, L22
Öberg, K. I., Guzmán, V. V., Furuya, K., et al. 2015, Natur, 520, 198
Okuzumi, S., Momose, M., Sirono, S.-i., Kobayashi, H., & Tanaka, H. 2016, ApJ, in press (arXiv:1510.03556)
Paardekooper, S.-J., & Mellema, G. 2006, A&A, 453, 1129
Qi, C., D'Alessio, P., Öberg, K. I., et al. 2011, ApJ, 740, 84
Qi, C., Wilner, D. J., Aikawa, Y., Blake, G. A., & Hogerheijde, M. R. 2008, ApJ, 681, 1396
Qi, C., Öberg, K. I., Wilner, D. J., et al. 2013, Sci, 341, 630
Rapson, V. A., Kastner, J. H., Millar-Blanchaer, M. A., & Dong, R. 2015, ApJL, 815, L26
Rybicki, G. B., & Lightman, A. P. 1979, Radiative Processes in Astrophysics (New York: Wiley)
Sirono, S.-i. 2011, ApJ, 735, 131
Takeuchi, T., Clarke, C. J., & Lin, D. N. C. 2005, ApJ, 627, 286
Thalmann, C., Carson, J., Janson, M., et al. 2009, ApJL, 707, L123
Turner, B. E. 1991, ApJS, 76, 617
Watanabe, N., & Kouchi, A. 2008, PrSS, 83, 439
Walsh, C., Juhász, A., Pinilla, P., et al. 2014b, ApJL, 791, L6
Walsh, C., Millar, T. J., & Nomura, H. 2010, ApJ, 722, 1607
Walsh, C., Millar, T. J., Nomura, H., et al. 2014a, A&A, 563, A33
Williams, J. P., & Best, W. M. J. 2014, ApJ, 788, 59
Zhang, K., Bergin, E. A., Blake, G. A., et al. 2016, ApJL, 818, L16